

Characterization of Multilayer Anti-Fog Coatings

Pascale Chevallier,^{†,‡} Stéphane Turgeon,[†] Christian Sarra-Bournet,^{†,‡} Raphaël Turcotte,^{†,‡} and Gaétan Laroche^{*,†,‡}

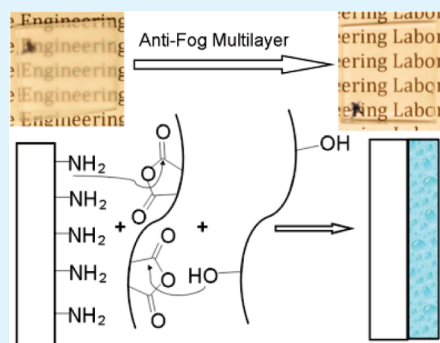
[†]Centre de Recherche du C.H.U.Q., 10 rue de l'Espinay, Québec, Québec G1L 3L5, Canada

[‡]Laboratoire d'Ingénierie de Surface (LIS), Centre de Recherche sur les Matériaux Avancés (CERMA), Département de Génie des Mines, de la Métallurgie et des Matériaux, Université Laval, Québec, Québec G1K 7P4, Canada

S Supporting Information

ABSTRACT: Fog formation on transparent substrates constitutes a major challenge in several optical applications requiring excellent light transmission characteristics. Anti-fog coatings are hydrophilic, enabling water to spread uniformly on the surface rather than form dispersed droplets. Despite the development of several anti-fog coating strategies, the long-term stability, adherence to the underlying substrate, and resistance to cleaning procedures are not yet optimal. We report on a polymer-based anti-fog coating covalently grafted onto glass surfaces by means of a multistep process. Glass substrates were first activated by plasma functionalization to provide amino groups on the surface, resulting in the subsequent covalent bonding of the polymeric layers. The anti-fog coating was then created by the successive spin coating of (poly(ethylene-maleic anhydride) (PEMA) and poly(vinyl alcohol) (PVA) layers. PEMA acted as an interface by covalently reacting with both the glass surface amino functionalities and the PVA hydroxyl groups, while PVA added the necessary surface hydrophilicity to provide anti-fog properties. Each step of the procedure was monitored by XPS, which confirmed the successful grafting of the coating. Coating thickness was evaluated by profilometry, nanoindentation, and UV visible light transmission. The hydrophilic nature of the anti-fog coating was assessed by water contact angle (CA), and its anti-fog efficiency was determined visually and tested quantitatively for the first time using an ASTM standard protocol. Results show that the PEMA/PVA coating not only delayed the initial period required for fog formation but also decreased the rate of light transmission decay. Finally, following a 24 hour immersion in water, these PEMA/PVA coatings remained stable and preserved their anti-fog properties.

KEYWORDS: plasma functionalization, thin films, anti-fog properties, polymer coatings, polyanhydride, poly(vinyl alcohol), surface characterization, coating stability



1. INTRODUCTION

Recent studies have explored various techniques to improve optical devices.^{1–5} Fog formation on surfaces is a definite concern, as fog reduces the effectiveness of light transmission and therefore optical efficiency.⁴ This hindrance is particularly disabling for such optical materials as eyeglasses, goggles, face shields, binoculars, not to mention analytical and medical instruments. As this fog occurs when water vapor condenses onto surfaces to form discrete and dispersed light-diffusing water droplets, the approach used most often for fog prevention is to increase the surface energy. Indeed, water condensation in contact with hydrophilic materials produces a continuous, transparent film.⁴

Over the last three decades,^{6–14} one common method to obtain hydrophilic surface properties has been thin film deposition using polymers or monomers containing hydrophilic functionalities, such as hydroxyl (OH) or carboxyl groups (COOH, COOR). For example, coatings have been made with poly(ethylene glycol),¹⁵ poly(vinyl alcohol) (PVA),^{10–12,15–18} poly(vinyl acetate),^{16,19–21} cellulose ester or cellulose ether,^{15,16}

acrylic resin with pending OH or COOH groups,^{15,22,23} glycidyl derivatives,^{24,25} or poly(vinyl pyrrolidone).^{6–8} However, because these anti-fog coatings are highly hydrophilic, they are also soluble in water. In order to maintain long-term anti-fog properties and enhance coating stability, reticulation agents are often used, resulting in a crosslinked polymeric network. These crosslinking agents may be organic or inorganic compounds or a mixture of both, such as polyisocyanate,^{6,7,15} glycol derivatives,²² acrylamide and epoxy resins,^{15,24} aluminium derivatives,¹⁶ or a combination of formaldehyde and zirconium nitrate.¹² Reticulation takes place through either UV irradiation^{15,22,24,25} or heating.^{10,11,16} However, while these coatings are well-crosslinked and cohesive, their weak adhesion to the substrate depends solely on the physical interaction between the two materials.

Received: November 11, 2010

Accepted: February 2, 2011

Published: March 07, 2011

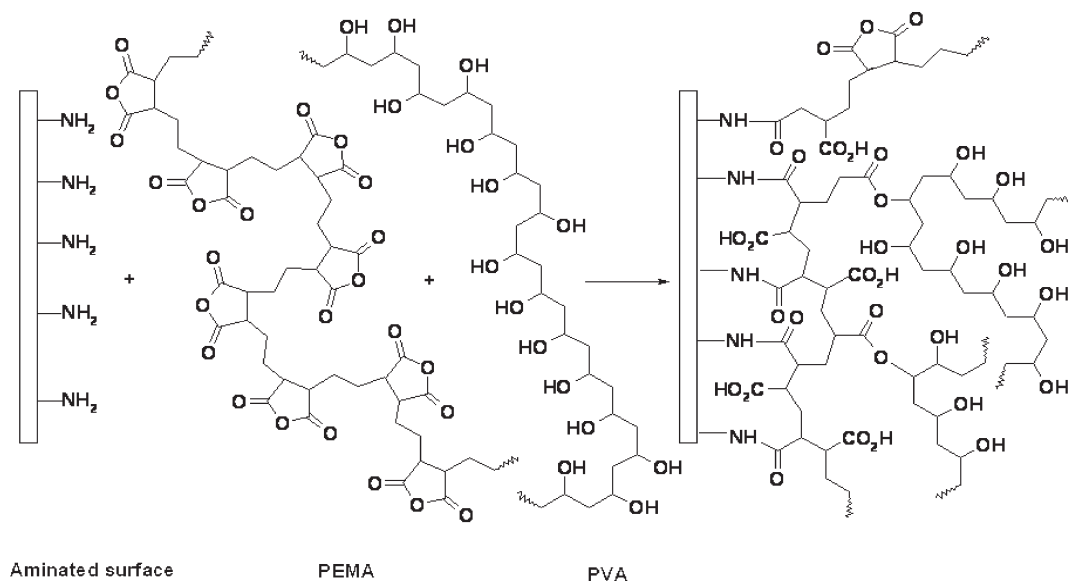


Figure 1. Multistep process for producing the anti-fog coating.

Our original approach consisted of covalently binding an anti-fog film on surfaces to obtain a stable as well as transparent anti-fog coating. With this in mind, glass surfaces were first activated by plasma functionalization to produce surface amino groups, which were further used as anchoring points for the covalent grafting of the anti-fog film. The anti-fog properties were provided by the alcohol functionalities of poly(vinyl alcohol). In order to bind the PVA to the glass surface amino groups, an intermediate polymer was chosen. Polyanhydrides were deemed as the ideal candidates, as anhydride groups are known to react with both amino and alcohol groups.^{26,27} In addition, because of their high-density anhydride groups, these polymers are known to induce crosslinkage,^{26–32} thus ensuring excellent cohesion of the multilayer assembly. Indeed, Figure 1 shows that some of the anhydride moieties of these polymers reacted with the surface amino functionalities, while some of the remaining anhydride groups reacted with the alcohol moieties. This novel approach may also be used to add subsequent layers of polyanhydride/poly(vinyl alcohol).

Surface modification and grafting performance was evaluated by X-ray photoelectron spectroscopy (XPS). Coating thickness (which should remain in the order of $\lambda/4$ to prevent refraction-induced visible light interference) was assessed by profilometry, nanoindentation, and UV–visible spectroscopy, while its roughness was determined by atomic force microscopy (AFM). Finally, fog formation was ascertained either visually, by photographing samples submitted to a cold–warm cycle, or quantitatively, by means of an ASTM standard protocol.³³ Despite the fact that several attempts to develop anti-fog coatings have been described in the literature, it is, to the best of our knowledge, the first time that such a quantitative procedure has been utilized to quantify the anti-fog properties of transparent samples.

2. MATERIALS AND METHODS

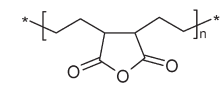
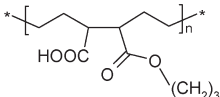
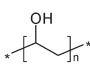
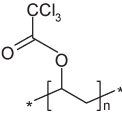
2.1. Materials and Sample Preparation. Fused silica slides measuring 2.5 cm \times 2.5 cm \times 2.5 mm were purchased from Technical Glass Products, Inc. (Painesville, OH, U.S.A.). Fused silica was used as the glass model because of its UV and visible light transparency as well as its high purity, as it contains no potentially soluble components, contrary

to other glass substrates. All of the chemical products were used as received. The H₂O₂ (33% wt), concentrated H₂SO₄, tetrahydrofuran (THF), chlorobenzaldehyde, chloropropanol, trichloroacetic anhydride, poly(ethylene-alt-maleic anhydride), $M_w = 100,000–500,000$, and poly(vinyl alcohol), 98% hydrolyzed $M_w = 84,000–124,000$, were all purchased from Sigma-Aldrich (Oakville, ON, Canada), while the acetone was purchased from Laboratoire Mat (Québec, QC, Canada). The Zero-Fog commercial anti-fog spray was obtained from OMS OptoChemicals (Montréal, QC, Canada).

2.2. Surface Modifications. The anti-fog layer grafting process consisted of three steps:

1. Fused silica materials were cut into 10 mm \times 10 mm samples, which were successively cleaned in ultrasonic baths containing acetone, deionized water, or isopropanol, followed activation by means of a piranha solution (mixture of 3 mL of H₂O₂ (33% wt) and 7 mL of concentrated H₂SO₄) for 15 min also in an ultrasonic bath. The surfaces were then ultrasonically cleaned three times in water for 10 min and in acetone for 2 min. Finally, the activated surfaces were dried under vacuum for 30 min prior to use. This so-called piranha treatment enabled hydroxylation of the fused silica surfaces.
2. To convert the surface hydroxyl functionalities into amino groups, the hydroxylated surfaces were placed in a commercial microwave (MW) plasma reactor from Plasmionique, Inc. (Varennes, QC, Canada). The surface activation was performed in the downstream region of the plasma consisting of high purity hydrogen and nitrogen (50%, 50%) at 300 W, 2.45 GHz, and 500 mTorr for 600 s.
3. Poly(ethylene-alt-maleic anhydride) (PEMA) was prepared at 0.1% (w/v) in a mixture of acetone and THF (1/2), while poly(vinyl alcohol) (PVA) solutions were prepared with 1% (w/v) of the polymer in water. First, the PEMA solution was spin coated at 2000 rpm during 20 s (spin coater WS-400-6NPP-LITE, Laurell Technologies, Inc., North Wales, PA, U.S.A.) and was allowed to cure at 95°C overnight under vacuum. Under these conditions, the anhydride functionalities of the polymer were expected to react with the surface amino groups on the fused silica. Thereafter, the surface was coated with a solution of 1% PVA at 4000 rpm for 30 s. Finally, the surface was cured for 6 h under vacuum at 95°C. The resulting coating is referred to as the 1-layer sample.

Table 1. Chemical Structures PEMA and PVA before and after Derivatization Reaction and Expected XPS Survey Concentration Values

	Chemical structure	Theoretical XPS composition		
		% C	% O	% Cl
PEMA		67.7	33.3	
PEMA + Cl-(CH ₂) ₃ -OH		64.3	28.6	7.1
PVA		67.7	33.3	
PVA + (Cl ₃ C-CO) ₂ O		22.2	44.5	33.3

Multilayered coatings were subsequently obtained by spin coating the PEMA (without curing), followed by the PVA, and finally curing the PEMA/PVA assembly for 6 h at 95°C. Additional layers were added by repeating this procedure.

2.3. Anti-Fog Ageing Tests. Each coated sample was aged in deionized water for 24 h at room temperature then dried under ambient conditions in order to test the coating's adhesiveness as well as optical/anti-fog stability on the fused silica substrate.

2.4. Surface Characterization. Following each step of the fused silica surface modification, the surface chemical composition was investigated by means of XPS using a PHI 5600-ci spectrometer (Physical Electronics, Eden Prairie, MN, U.S.A.). A standard aluminum X-ray source (1486.6 eV) was used at 300 W with a neutralizer to record the survey spectra, and the high resolution spectra were obtained by using a standard magnesium X-ray source (1253.6 eV) at 300 W with no charge neutralization. Photoelectron detection was generally performed at 45° with respect to the surface plane; however, angle-resolved XPS (ARXPS) was also performed by varying the angle between the detector and the surface plane from 15° to 90°.

Amine surface concentration was quantified through a vapor phase chemical derivatization technique using chlorobenzaldehyde, which has been previously described.³⁴ Briefly, derivatization reactions were performed for 2 h at 40°C in a sealed glass tube in which a 1 cm thick bed of soda–lime glass beads was introduced to separate the reagent from the reactive surfaces. The surfaces were then outgassed overnight under vacuum and subsequently analyzed by XPS. Similar procedures were performed at room temperature using either chloropropanol or trichloroacetic anhydride to determine the availability of anhydride groups from the PEMA and alcohol groups from the PVA, respectively. Table 1 presents the chemical structures and expected atomic surface concentration values before and after the derivatization reactions, considering reaction rates of 100%.

Static contact angle measurements of the samples were recorded using a VCA 2500 XE system (AST, Billerica, MA, U.S.A.). A total of 3 μL of deionized water were deposited on the surface with a constant flow of 6 μL/min. The contact angles were measured on three drops randomly deposited on different parts of each sample, followed by triplicate analyses.

Atomic force microscopy (AFM) investigations were performed using a Dimension 3100 atomic force microscope (Digital Instruments,

Santa Barbara, CA, U.S.A.) in tapping mode with an etched silicon tip (OTESPA, tip radius <10 nm, aspect ratio ≈1.6/1). Surface topography was evaluated for areas covering 20 × 20 μm² using the Nanoscope program. The AFM images were analyzed using the WSxM 3.0 Beta 12.4 Image Browser software,³⁵ and the surface roughness was determined using the root mean square roughness parameter R_{rms}.

Thickness measurements were performed using the same AFM in nanoindentation mode with a Berkovich diamond indenter tip (radius of <50 nm, Veeco, Santa Barbara, CA, U.S.A.) according to the manufacturer's instructions. Ten increasing forces were applied per line, with three lines per analysis (Figure S1a of the Supporting Information). Briefly, the penetrating depth of the nanoindenter tip varied somewhat linearly with the applied force until reaching a plateau (identified by the black, green, and red arrows (Figure S1a of the Supporting Information), which shows the point where the tip reached the fused silica surface. The thicknesses are the mean nanoindenter tip penetration depths measured at the so-called plateau from three different linear patterns (Figure S1b of the Supporting Information). Again, these analyses were performed in triplicate. Film thickness was also measured with a TENCOR P2 stylus profilometer (SPEC, Santa Clara, CA, U.S.A.) at a vertical resolution of 25 Å for the glass samples.

UV–vis transmission spectra of 1–8 layers (PEMA/PVA) on the glass substrates were acquired on a UV 1600 spectrometer (Shimadzu, Kyoto, Japan) from 200 to 800 nm. Background spectrum acquisition was performed on an uncoated substrate. Following the method suggested by Swanepoel,³⁶ the interference fringe patterns were used to determine the thickness of the first and subsequent layers, after which time the different extrema in each layer (from 3 to 8) were ascertained from the transmission spectrum. In order to minimize the effects of noise and absorbance-related slope, a polynomial function was first fitted around the visually determined position of each extremum, after which the position of the absolute maximum of the second derivative of this polynomial (hence, the maximum curvature) was used as the position of the interference fringe extremum (Table S1 of the Supporting Information). By defining $l/2$ as the interference order, and by assigning an even l number to each maximum and an odd l number to each minimum, the thickness of the layer referred to as d was therefore calculated as follows³⁶

$$l/2 = 2d \times (n/\lambda) \quad (1)$$

where λ is the wavelength of the maxima and minima and n is the refractive index at that wavelength (Figure S2a of the Supporting Information).

Therefore, the resulting plots for each layer led to straight lines with a slope of $2d$ (eq 1), where d is the thickness of the layer (Figure S2b of the Supporting Information).

2.5. Fog Evaluation and Fog Quantification. The fog formation on various samples was first evaluated by visual inspection of surface photographs taken immediately after a cold–warm transition, which consisted of placing samples in a cold chamber at –20°C for 30 min then bringing them back to room temperature.

Quantification of the fog was then performed using a Fog Quantification Box (FQB; Figure 2), which was constructed according to ASTM F 659-06³³ and its equivalent European versions BS EN 166-168. Each optical component was purchased from Edmund Optics (Barrington, NJ, U.S.A.). The light source, a 590 nm collimated microscope LED (LEDC21, Thorlabs, Newton, NJ, U.S.A.), generating a large 30 mW beam, was directed into a 1 cm diameter iris diaphragm (I1). The beam was then brought to the sample through a 50/50 beam splitter (BS) and a series of 45° mirrors (M2-4). The sample was placed on a 1 cm² aperture made on an opaque box 2.54 cm in height. The box itself stood on a thermostatic bath filled with water heated to 50°C. The bath was large enough to contain at least 4 L of air over the water. A mirror (M1) placed at the bottom of the bath reflected the perpendicular incident

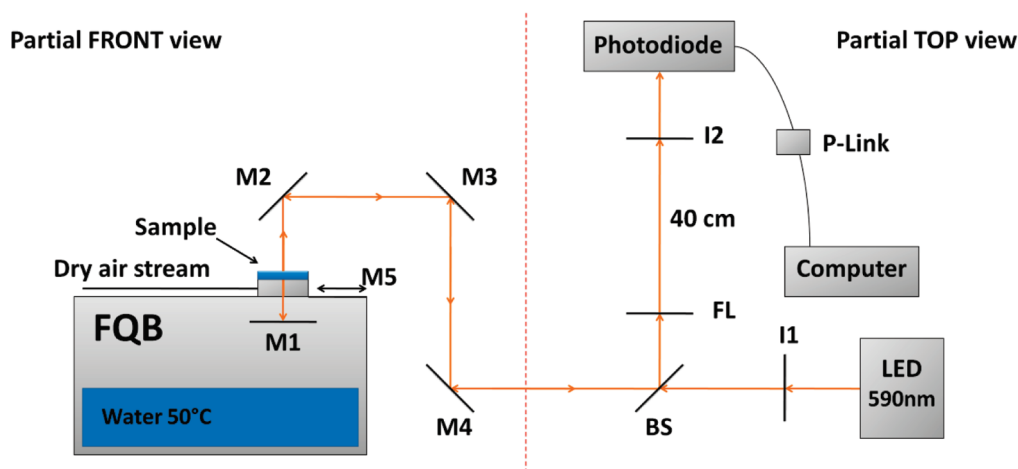


Figure 2. Apparatus used to quantify the anti-fog properties according to the ASTM F 659-06 protocol; M, mirrors; I, iris diaphragm; FL, focal lenses; BS, beam splitter; LED, light-emitting diode; and P-Link, laser power meter.

light back to the sample. The epi-directed beam was then directed by the 50/50 beam splitter (BS) to a focal lens (FL, $f = 40$ cm) and focused at a second iris diaphragm (I2) behind which an Si photodiode (PH100-Si, Gentec-ElectroOptics, Québec, QC, Canada) was immediately positioned for light detection.

The distance between the sample and the FL was kept short enough for the light that was deviated 15° by the fog to reach the clear aperture of the FL and thus be detected. A sliding mirror door (M5) isolated the sample from the hot water bath, making it possible to measure the light intensity transmitted through the sample before exposure to the humidity. To ensure better isolation, a gentle dry air stream at 20°C was introduced into the sample box. The photodiode was connected to a computer via a laser power meter (P-Link, Gentec-ElectroOptics) for data storing and analysis. Data were continuously saved to simplify the measurements.

The fog measurements were completed once using three samples per condition. The presented results are therefore the mean values of the three samples for each condition.

3. RESULTS AND DISCUSSION

3.1. Chemical Composition. XPS analyses enabled us to follow each step of the surface modification process. Piranha and MW plasma treatments were performed successively to break the Si–O–Si bonds in Si–OH and to substitute the newly formed hydroxyl functionalities with amino groups.³⁷ The XPS results clearly confirm the effectiveness of both treatments, as the piranha treatment led to a 10% increase in the oxygen relative surface concentration (Figure 3a), and 2% nitrogen was detected following the MW plasma treatment (Figure 3a). Moreover, $\sim 65\%$ of the nitrogen introduced onto the surface upon MW plasma were amino groups,³⁷ as deduced from the XPS survey spectrum following the chemical derivatization with chlorobenzaldehyde (1.5% of Cl – Figure 3d). These amino functionalities were thus used to graft the polyanhydride (PEMA).

The effectiveness of the PEMA coating was also clearly evidenced by the XPS data, which showed a decrease in the silicon XPS feature concomitant with an increase in the carbon surface content (Figure 3b). The “expected” unreacted anhydride functionalities of the PEMA were then brought to react with the alcohol groups of the PVA upon further spin coating of this polymer solution onto the sample surfaces (Figure 1). The

XPS survey spectra, however, did not enable a direct detection of PVA on the surface, as both PEMA and PVA displayed identical chemical compositions (Table 1). Nevertheless, the decreased silicon surface concentration from 10% after PEMA grafting to 2.1% after PVA coating, with a concomitant increase in the C1s XPS feature, constitutes a clear indication of a successful PVA coating. The XPS HR spectra also confirm this conclusion. Indeed, the HR C1s XPS spectra clearly made it possible to distinguish the different chemical bonding through their binding energy shifts (Figure 3c). The PEMA coating exhibited a band at 289.7 eV characteristic of anhydrides $-(\text{CO})_2\text{O}$ (Figure 3c). Following the single-layer PVA coating (Figure 3c), the HR C1s spectrum displayed a very different band shape with the appearance of a peak at 286.6 eV attributed to the $\text{C}-\text{O}$ band from alcohol. Moreover, the reaction of the anhydride groups with the alcohol functionalities led to the formation of esters, clearly evidenced by the presence of the band at 287.8 eV ($-\text{CO}_2-$).

The aforementioned hypothesized presence of unreacted anhydride groups following the PEMA coating was further ascertained by means of surface derivatization using chloropropanol. Following this derivatization, the recorded XPS spectrum revealed the detection of 4.3% chlorine (Figure 3d), thereby supporting the fact that some anhydride functions remained available despite the prior reaction with surface amino groups on the fused silica. Simple calculations made while considering a 100% complete reaction between the chloropropanol and the PEMA enabled us to determine that a maximum Cl surface concentration of 7.1% may have been detected (Table 1 : PEMA + Cl(CH₂)₃-OH). The measured value of 4.3% signifies that $\sim 60\%$ of the total amount of anhydride groups in the PEMA remained available for reaction with the alcohol moieties of the PVA. This may be explained by the prior anhydride reaction with amino groups on the fused silica as well as the steric hindrance due to the high molecular weight of the PEMA ($M_w = 100,000 - 500,000$).

Similarly, the presence of alcohol moieties on the complete anti-fog layer (PEMA + PVA) was determined by surface derivatization using trichloroacetic anhydride. In this case, the anhydride functionalities reacted with the expected free surface alcohol groups from the PVA, resulting in the formation of an ester linkage. Following this reaction, we recorded 21.6% chlorine atoms (Figure 3d). Again, a theoretical 100% complete

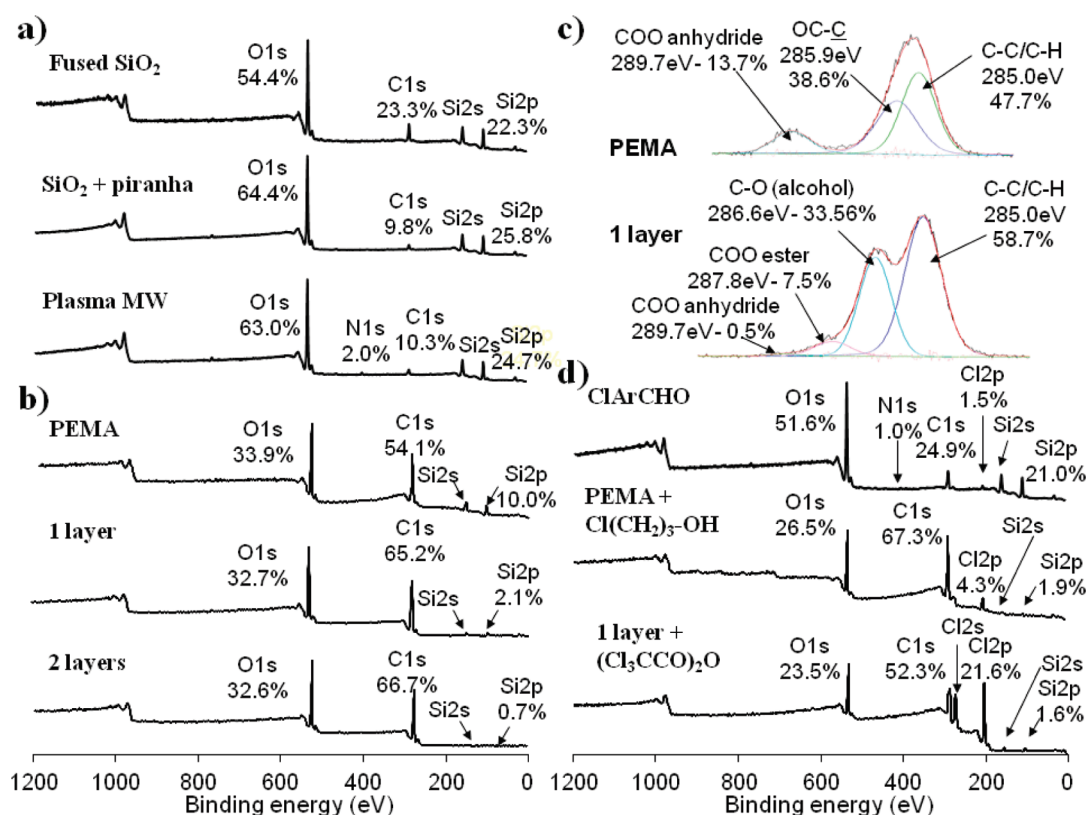


Figure 3. XPS survey spectra at different steps during the surface modification of (a) the fused silica surface, its activation by piranha solution, and MW plasma treatment; (b) after PEMA, PEMA/PVA (1 layer), and (PEMA/PVA) \times 2 (2 layers) grafting; (d) after chemical derivatization with the appropriate chemical reagents to quantify amino group surface concentration on the MW plasma-treated fused silica, PEMA-coated surfaces, and PEMA/PVA-coated surfaces; (c) C1s high resolution spectra after PEMA and PVA grafting.

reaction between the trichloroacetic anhydride and the PVA would have produced a chlorine surface concentration of 33.3% on the PVA (Table 1: PVA + $[\text{Cl}_3\text{C}-\text{CO}]_2\text{O}$), thus enabling us to conclude that 65% of the alcohol groups of the PVA in the PEMA/PVA coating remained unreacted.

XPS detection (at 45°) of silicon on either the 1- or 2-layer samples (Figure 3b) raised a concern regarding coating homogeneity, as the presence of defects or porosity may lead to such an observation and extreme thinness may also produce similar results. ARXPS provides an initial approximation of the various layer thicknesses because the photoelectron depth of origin decreases with the photoelectron detection angle with respect to the surface plane. In this instance, it was estimated that for C1s and O1s, the depth at which 95% of the detected XPS signals originated was ~ 4.5 – 6.0 nm for normal emission (at 90°) and ~ 1.0 – 1.5 nm for grazing emission (at 15°).^{38,39} As no difference in chemical composition was observed for detection at 90° , the coating thickness was higher than 4–6 nm and defects/porosity were present in these films.

In addition, ARXPS analysis of the survey spectra of a sample made of a single PEMA coating on the fused silica detected 5.2% Si, with 13% detected at 90° . This observation was further confirmed through the ARXPS C1s HR spectra, which revealed 21 and 9.9% C originating from the anhydride moieties at detection angles of 90° and 15° , respectively. These data indicate that the PEMA coating was thinner than 4–6 nm, while taking into account the possible presence of porosity. This is in agreement with previous literature^{40–44} in which coating thicknesses ranging from 4 to 8 nm were obtained from spin coating

Table 2. Thickness of 1–8 Layers of Anti-Fog Coating Measured by (A) Profilometry and (B) Nanoindentation

number of layers	1	2	3	4	6	8
A	39 \pm 5	76 \pm 5	103 \pm 9	131 \pm 7	212 \pm 6	255 \pm 7
B	43 \pm 3	75 \pm 3				

PEMA polymer solutions with concentrations similar to those used in the present study. These ARXPS data warranted further characterization of the thickness and morphology of the anti-fog coating.

3.2. Film Thickness and Morphology. Stylus profilometry experiments were performed on the fused silica samples coated with 1–8 layers of the anti-fog treatment to characterize the thickness of each coating layer. As shown in Table 2, the profilometry results clearly demonstrate that thickness was directly correlated to the number of deposited layers, with an average layer thickness increase of 33.3 nm per layer ($r^2 = 0.9876$). Of interest is that the first layer was slightly thicker (~ 39 nm) than each subsequent layer (~ 33 nm). This may be explained by the fact that the first layer was in direct interaction with the fused silica surface, while the other layers were able to interpenetrate with the layer underneath.

The profilometry data were further confirmed by means of nanoindentation experiments. Briefly, increasing forces were applied to a nanoindenter tip, resulting in different penetration depths. When the tip reached the fused silica surface, a plateau was reached, whereas applying additional pressure on the tip led to a breaking of the fused silica surface and hence, to a further

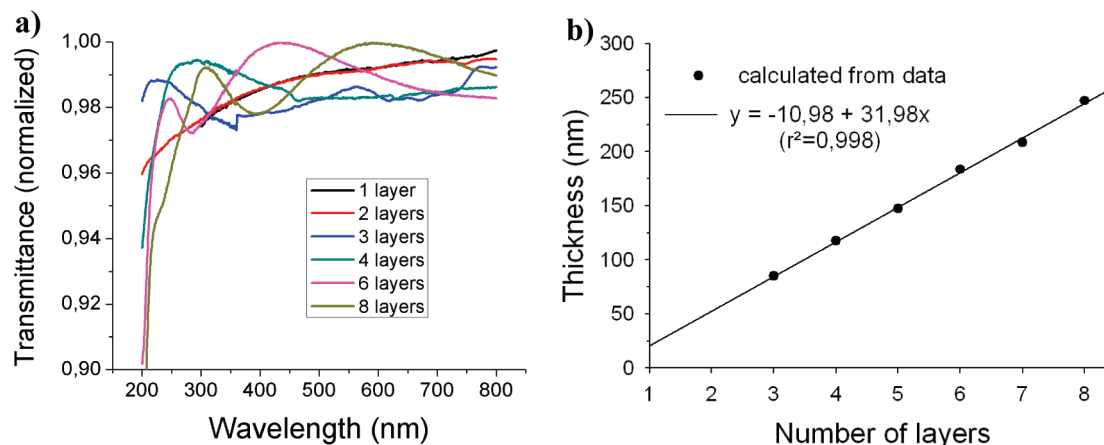


Figure 4. (a) UV–visible transmission spectra and (b) thickness as a function of the number of layers.

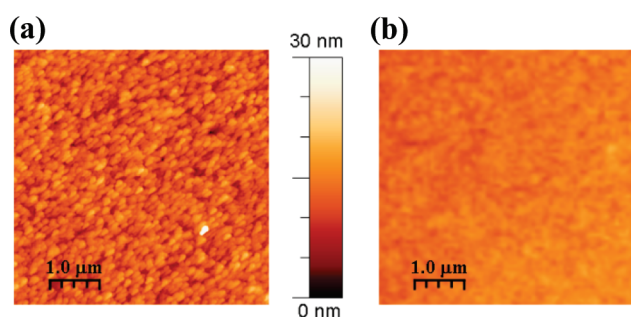


Figure 5. $5 \mu\text{m} \times 5 \mu\text{m}$ AFM images of (a) PEMA 0.1% w/v coating on MW plasma-treated FS after curing and (b) PEMA/PVA coating after curing (leading to the so-called 1-layer coating).

penetration of the tip within the glass substrate (Figure 1a of the Supporting Information). Thus, the thickness data presented in Table 2 are the mean nanoindenter tip penetration depths measured at this plateau from three different linear experiment patterns. Of interest is that the coatings made with more than three anti-fog layers were shown to be too thick to be measured by nanoindentation.

UV–vis spectra of the 1–8 layer coatings were also recorded. The primary objective being to ascertain whether light transmission was not overly affected by the presence of the polymers. As clearly demonstrated in panel (a) of Figure 4, light transmission remained very high in the visible spectral region, with values ranging from 95 to 100%, regardless of the number of anti-fog layers. UV–vis spectroscopy also proved to be a powerful and nondestructive tool to measure coating thickness. As shown in panel (a) of Figure 4, the spectrum of the single layer is largely superimposed by that of the double layer, except between 200 and 300 nm. This spectral region proved too difficult to reliably acquire, most likely due to the porosity of the single layer observed by AFM (Figure 5) and corroborated by Si detection under XPS. The same cause prevented any interference pattern on the spectra of both the single and double layers. The spectrum of the double layer may therefore be used to determine the average refractive index of the material as a function of wavelength,³⁶ although this data may be used only in the transparent region (400–800 nm). Following the Swanepoel procedure,³⁶ an inverse second order polynomial function was fitted to this data and extrapolated to obtain the values from 200 to 400 nm. The resulting refractive index curve (Figure S2a of the

Table 3. Roughness and Contact Angle Measurements^a

	FS-pir	FS-MW	PEMA 0.1%	1 layer	2 layers
R_{rms} (nm) $20 \mu\text{m} \times 20 \mu\text{m}$	1.6 ± 0.1	1.1 ± 0.3	5.3 ± 0.4	1.5 ± 0.6	2.7 ± 0.9
CA (deg)	29 ± 3	17 ± 3	51 ± 3	42 ± 4	53 ± 5

^aFS-pir: fused silica treated by piranha. FS-MW: microwave plasma-treated fused silica. PEMA: fused silica coated with PEMA alone. 1 layer: fused silica coated with PEMA/PVA. 2 layers: fused silica coated with (PEMA/PVA) \times 2.

Supporting Information) was thereafter used to calculate the thickness of the PEMA/PVA coating as a function of the number of layers deposited on the silica samples (Figure 4b). Of interest is that the refractive index values 1.15–1.2 (Figure S2a of the Supporting Information) were rather low compared to the tabulated values of 1.5 for both PEMA and PVA in other studies.^{42,45} This difference again suggests the presence of porosity in the layers, which lowered the average value of the refractive index.

The calculated straight line indicates that the (apparent) thickness of a single PEMA/PVA coating was 21 nm, with a slope of 32 nm corresponding to the thickness of the subsequent layers. The latter value is in perfect agreement with the profilometry and nanoindentation data of 33.3 and 32.1 nm, respectively. Of note, the thickness values obtained for the single and double layers were smaller than the profilometry and nanoindentation values because of the porosity of these layers; contrary to profilometry and nanoindentation techniques, optical thickness measurements are influenced by porosity.

Together with the coating thickness data (whether measured by profilometry, nanoindentation, or UV–vis transmission), the XPS results show that the anti-fog coating was porous to a certain degree. Indeed, this statement is supported by the fact that the XPS spectra of the samples coated with one or two anti-fog layers were almost identical and made it possible to detect silicon in the fused silica substrate underneath. In addition, the low refractive index of ~ 1.2 (Figure S2a of the Supporting Information) deduced from the UV–vis spectra was somewhat indicative of the presence of porosity in the layers, although the AFM data did appear to contradict these assertions, as the 1- and 2-layer anti-fog coatings exhibited a very low surface roughness (Table 3).

An explanation for these apparent contradictory results stems from the step-by-step AFM analysis upon creating the anti-fog layer. Indeed, the spreading of a single PEMA layer onto the fused silica led to the formation of small circular beads stacked together (Figure 5a). This globular shape of dried polymer chains with a dense surface coverage was already observed by Pompe et al.⁴⁶ This therefore explains the high level of silicon still detectable by XPS after the fused silica was coated with a single PEMA layer (Figure 3b). Coating this “stacked bead” structure with PVA minimized the surface roughness measured by AFM (Table 3), while entrapping this porous structure within the coating (Figure 5b). In light of this, if the ultimate goal is to minimize light diffusion artifacts, the decreased surface roughness provided by the PVA coating is of paramount importance for optical applications. These overall data made it possible to rule out the presence of non-homogeneous features within the coating structure and rather point to porosity, which was randomly distributed within the PEMA/PVA assembly.

The anti-fog nature of a surface is driven by its hydrophilicity.⁴ Indeed, the equilibrium of a droplet in contact with a surface, as described by Young's equation,⁴⁷ is the primary factor to determine whether a condensed fluid will fog a surface. Generally speaking, surfaces with low contact angles allow water to form a homogeneous film on the surface rather than multiple circular drops; the former situation is by far preferred to preserve optical transmission.⁴ Table 3 presents the results of the contact angle analyses.

The reference substrate (namely, fused silica treated in piranha solution) exhibited a contact angle of 29°, while its microwave plasma treatment brought this value down to 17°, likely because of the conversion of the hydroxyl groups into amino functionalities. Coating the microwave-treated fused silica with PEMA provided the surface with greater hydrophobic properties because of the presence of the polymer ethylene groups and the roughness of this coating (Table 3). The contact angle measured for this surface was therefore 51°, in agreement with previously reported values ranging between 52° and 57°.^{40,42,44,48} The hydrophilic nature of PVA provided a contact angle of 42° for the sample coated with one layer and 53° for the sample coated with two layers. These values are somewhat surprising for anti-fog coatings, considering other reported values closer to 40°.^{4,47,49} These rather elevated contact angle values can be explained by considering the various mathematical equations developed to describe the wetting phenomenon. As pointed out by Marmur,⁵⁰ the Wenzel equation is based on the assumption that wetting is homogeneous and therefore predicts a decrease in contact angle with roughness/porosity. In contrast, the Cassie-Baxter equation was developed to take heterogeneous wetting into account in the particular case where air bubbles are trapped underneath the liquid. According to Figure 5, the type of topography of the PEMA surface (protrusions with comparatively narrow pits) does indeed satisfy the conditions determined by Marmur⁵¹ as leading to heterogeneous wetting, hence air trapping, hence increased contact angle.

3.3. Anti-Fog Properties. One way to characterize the anti-fog properties of coatings is simply to stabilize the temperature of treated materials placed in a cold chamber (−20°C) for 1 h, then return them to ambient conditions, as the thermal gradient provides good conditions for drop-moisture formation. As shown in Figure 6, the 1- and 2-layer samples remained fog-free, whereas the fused silica (Figure 6A) and the PEMA coating (Figure 6B) were fully fogged. This test clearly shows that the

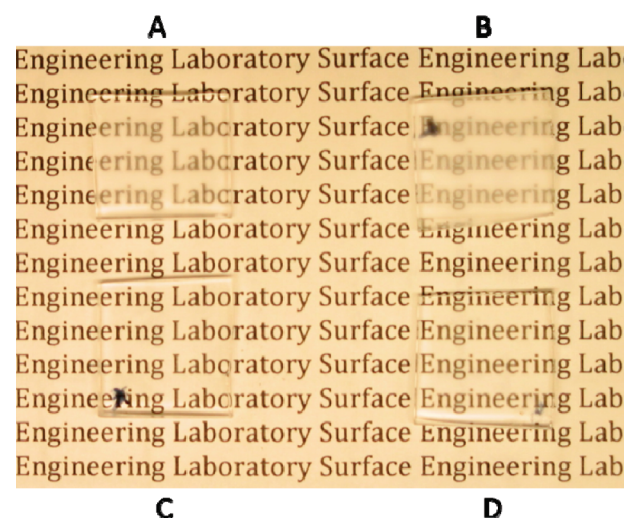


Figure 6. Photographs of samples submitted to a cold–warm transition (surfaces were placed in a cold chamber for 1 h and brought back to room temperature immediately before being photographed). (A) fused silica, (B) fused silica coated with PEMA alone, (C) 1 layer, fused silica coated with PEMA/PVA, and (D) 2 layers, fused silica coated with (PEMA/PVA) × 2.

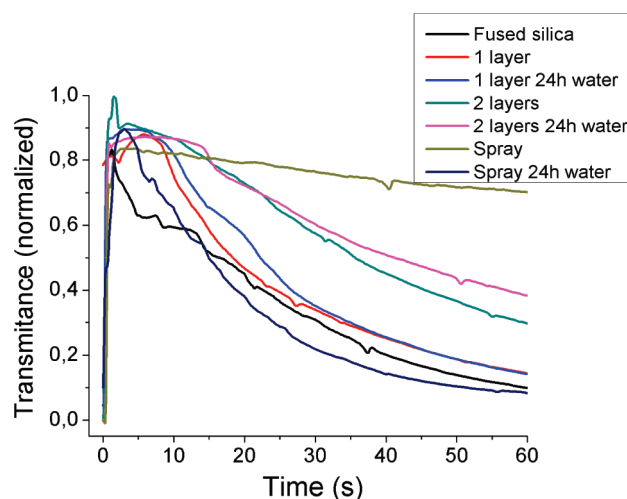


Figure 7. Light transmission over time through the fused silica samples according to the ASTM F 659-06 standard protocol.

sole presence of PEMA failed to provide anti-fog properties; these were only observed when the top coating was PVA because of its high hydrophilicity. Of interest is that the anti-fog features were conferred to both the single- and double-layer samples despite contact angles of 42° and 53° (Table 3). This observation may be explained by the PEMA coating's morphology (Figure 5a), as its circular shape induced greater roughness, which in turn produced a higher contact angle, despite the additional PVA coating displaying the hydrophilic and anti-fog properties.

As shown in Figure 6, the primary consequence of fog was the decrease in light transmission caused by light diffusion. Of note, photographs were also recorded after exposing the samples at −20 °C for 1 h hour, bringing them back to ambient conditions and immediately breathing on them (Figure S3 of the Supporting Information). Despite being more difficult to standardize than

Table 4. Typical data Measured from the Light Transmission Curves Presented in Figure 7^a

	FS	1 layer	1 layer 24 h water	2 layers	2 layers 24 h water	spray	spray 24 h water
decay (s^{-1}) \times 100	5.4	3.2	3.7	2.5	2.0	1.8	7.1
plateau width (s)	3.6	9.4	11.0	11.1	14.4	11.1	4.9
T after 30 s (%)	31	34	35	58	60	76	22

^aFS: fused silica.

the simple cold–warm transition tests, these experiments led to identical conclusions regarding the potential of PEMA/PVA coatings to prevent fog formation.

In order to quantify the results presented in Figure 6, the light transmission through samples as a function of time was monitored, while the samples were exposed to a humid atmosphere, as described in the standard ASTM procedure.³³ For comparison, a commercially available anti-fog spray was used as a reference. The 1 and 2 layers as well as the anti-fog spray-coated samples were also aged for 24 h in water to assess the coating stability and to ascertain whether their anti-fog properties were preserved following prolonged exposure to water.

The curves presented in Figure 7 were recorded immediately following exposure of the samples to the humid environment, which consisted of a heated water bath at 50°C. As shown, a typical curve profile first displayed a plateau (for which time duration was determined through a second derivative of the experimental curves) corresponding to the time for which the sample remained almost 100% clear despite being exposed to the humid atmosphere. During this period, a water monolayer formed on the surface, with no significant impact on the light transmission. What followed was a decay of the light transmittance due to excess water droplet formation. This decay can be quantified by fitting an exponential mathematical function with lower decay values corresponding to better anti-fog properties. Finally, the ASTM protocol states that an anti-fog material should retain 80% of its light transmission after 30 seconds of exposure to humidity.³³ Table 4 summarizes the characteristic anti-fog parameters.

As shown in Table 4, the worst anti-fog properties were recorded by the fused silica sample for which the light transmittance curve displayed a very short plateau region (3.6 s), a fast light transmission decay ($5.4 s^{-1}$), and only 31% of light transmission remaining after 30 s. In contrast, the best anti-fog coating was recorded by the commercially available spray with a plateau period lasting 11.1 s, a light transmission decay of $1.8 s^{-1}$, and 76% of light transmission remaining after 30 s.

The analysis of these curves also enabled us to conclude that the best anti-fog coating achieved in the present study was obtained by applying two layers of the PEMA/PVA anti-fog coating which delayed the time of fog formation (11.1 s), with a light transmission decay of $2.5 s^{-1}$ and a light transmission of 58% after 30 s of exposure to humidity. Despite being less efficient than the commercially available spray, the PEMA/PVA coatings not only clearly improved the anti-fog properties of the fused silica but clearly surpassed the commercial spray when the permanency of the anti-fog properties was taken into account. Figure 7 indeed confirms that the 2 layer sample maintained its anti-fog properties following a 24 hour immersion in water (confirmed by the XPS data showing no surface chemistry modification; data not shown), while a similar procedure performed on the sample treated with the commercial spray led to a full recovery of the same anti-fog properties as those of the untreated sample. Of interest is that none of the samples for which light transmission data are presented (Figure 7) met the ASTM anti-fog criteria. Quantifying the anti-fog properties of the

different coatings thus provided an objective quantitative comparison of their performance. To our knowledge, it is the first time that ASTM anti-fog characterization procedures have been used to quantify anti-fog properties. In this context, the best comparison with other anti-fog technologies developed thus far can only be achieved on a qualitative basis. Unfortunately, this assessment is shown to be useless, as all anti-fog coatings previously described in the literature behave fairly well when submitted to a cold–warm cycle, which therefore constitutes a rather easy demonstration. In this regard, the 60% light transmission after 30 s measured for the PEMA/PVA 2 layer sample using the ASTM protocol may thus be considered as the standard to beat. In addition, the need to covalently graft the anti-fog layer to the underlying surface in order to maintain its properties upon cleaning procedures has been clearly demonstrated.

4. CONCLUSION

A multistep anti-fog process was applied on fused silica. The activation of glass using a piranha solution followed by plasma functionalization enabled the grafting of 1.2% of amino groups on the fused silica surface. These nucleophilic moieties were then used to conjugate poly(ethylene-alt-maleic anhydride), which acted as both a linking arm and a crosslinker with the additional spin-coated poly(vinyl-alcohol) layer. We demonstrated that applying several layers of a PEMA/PVA coating improved the anti-fog properties of the fused silica. The techniques used to measure each PEMA/PVA layer thickness all provided similar results, with values approximating ~ 32 nm for each additional layer. Consequently, 1 or 2 layers of the entire PEMA/PVA coating assembly were thin enough to prevent it from causing a refraction-induced visible interference of the transmitted light. Despite contact angles greater than 40°, the PEMA/PVA coatings displayed interesting anti-fog properties, as evidenced either visually or quantitatively by a standard ASTM protocol. Moreover, the PEMA/PVA coatings remained intact and preserved their anti-fog properties even after a 24 hour immersion in water. Further research is ongoing to improve the PEMA/PVA coating morphology to minimize the presence of porosity.

■ ASSOCIATED CONTENT

Supporting Information. Additional nanoidentation images of the PEMA/PVA coating; data used to calculate the thickness of the PEMA/PVA layers by UV-vis; and photographs of samples cooled to -20°C for 1 h, returned to ambient conditions, and warmed under breathing. This information is available free of charge via the Internet at <http://pubs.acs.org/>.

■ AUTHOR INFORMATION

Corresponding Author

*E-mail: gaetan.laroche@gmn.ulaval.ca. Phone: (418) 656-2131, ext. 7983. Fax: (418) 656-5343.

ACKNOWLEDGMENT

The authors thank Louison Maechler and Nicolas Gherardi from the Université de Toulouse III; UPS, INPT; LAPLACE (Laboratoire Plasma et Conversion d'Énergie), France, for the profilometry measurements. They also acknowledge the financial support from the National Science and Engineering Research Council (NSERC) through its I2I program and the Centre québécois sur les matériaux fonctionnels (CQMF), Québec, Canada.

REFERENCES

- (1) Kuo, C.-Y.; Chen, Y.-Y.; Lu, S.-Y. *ACS Appl. Mater. Interfaces* **2008**, *1*, 72–75.
- (2) Shimomura, H.; Gemici, Z.; Cohen, R. E.; Rubner, M. F. *ACS Appl. Mater. Interfaces* **2010**, *2*, 813–820.
- (3) Cebeci, F. A.; Wu, Z.; Zhai, L.; Cohen, R. E.; Rubner, M. F. *Langmuir* **2006**, *22*, 2856–2862.
- (4) Howarter, J. A.; Yougblood, J. P. *Macromol. Rapid Commun.* **2008**, *29*, 455–466.
- (5) Zhang, L.; Li, Y.; Sun, J.; Shen, J. *Langmuir* **2008**, *24*, 10851–10857.
- (6) Creasy, W. S. Transparent Anti-Fog Coating Compositions. U.S. Patent 4,467,073, August 21, 1984.
- (7) Creasy, W. S. Hydrophilic Polyvinylbutyral Alloys. U.S. Patent 4,847,324, July 11, 1989.
- (8) Funaki, M.; Yoshida, M.; Shimauchi, Y.; Fujioka, A.; Sakiyama, K. Coated Materials and Production Thereof. U.S. Patent 4,242,412, December 30, 1980.
- (9) Haller, I. *J. Am. Chem. Soc.* **1978**, *100*, 8050–8055.
- (10) Hosono, H.; Taniguchi, T. Anti-Fogging Film. U.S. Patent 5,134,021, July 28, 1992.
- (11) Hosono, H.; Taniguchi, T.; Nishii, M. Process for Preparation of Anti-Fogging Coating. U.S. Patent 5,075,133, December 24, 1991.
- (12) Laurin, B. L. Abrasion and Antifog-Resistant Optical Element. U.S. Patent 4,127,682, November 28, 1978.
- (13) Petersen, N. E. Anti-Fogging Surgical Mask. U.S. Patent 4,419,993, December 13, 1983.
- (14) Sanders, J., A.J.; Larson, M. J. Transparent Anti-Fog Compositions. U.S. Patent 4,615,738, October 7, 1986.
- (15) Haga, M.; Onisawa, Y.; Shimizu, K. Plastic Lenses and Method of Producing the Same. U.S. Patent 5,985,420, November 16, 1999.
- (16) Song, J. C. Transparent Anti-Fog Coating. U.S. Patent 5,804,612, September 8, 1998.
- (17) Eggers, H.; Klein, R.; Muller, C.; Brandt, R. Multilayer Film with Lamination and Heat-Sealable Sides, And Having Antifogging Properties. U.S. Patent 6,576,348, December 12, 2002.
- (18) Murata, N.; Hirukawa, M.; Honjo, H.; Matsuura, T.; Yamazaki, S. Coating agent for forming antifogging film and method for forming antifogging film using same. U.S. Patent WO 2004/013063 A1, February 2, 2004.
- (19) Nagasawa, H.; Nakamura, M.; Ishida, M.; Ohsawa, H.; Hoga, T. Antifogging Agent Composition. U.S. Patent 2003/0127625 A1, July 10, 2003.
- (20) Yamazaki, S.; Murata, N.; Yamamoto, H. Article with Antifogging Film and Process for Producing Same. U.S. Patent 6,420,020 B1, July 16, 2002.
- (21) Yamazaki, S.; Murata, N.; Yamamoto, H. Article with Antifogging Film and Process for Producing Same. U.S. Patent 6,531,215, March 11, 2003.
- (22) Kruger, A. A.; Chartier, P. Anti-Fogging Coating Composition, Product Coated with Said Composition for Preparation of Said Product. U.S. Patent 5,578,378, November 26, 1996.
- (23) Keller, M.; Lenhard, M. Substrate and Polymerizable Mixture, Method of Manufacturing of Said Polymerizable Mixture, And Method of Manufacturing of a Nonfogging or Low Fogging Layer. U.S. Patent 5,648,441, July 15, 1997.
- (24) Oshibe, Y.; Yamamoto, Y.; Ohmura, H.; Kumazawa, K. Composition of Ultraviolet Curing Antifogging Agent and Process for Forming Antifogging Coating Film. U.S. Patent 5,244,935, September 14, 1993.
- (25) Oshibe, Y.; Yamamoto, Y.; Ohmura, H.; Kumazawa, K. Antifogging resin film-forming composition. U.S. Patent 5,180,760, January 19, 1993.
- (26) Chaix, C.; Minard-Basquin, C.; Delair, T.; Pichot, C.; Mandrand, B. *J. Appl. Polym. Sci.* **1999**, *70*, 2487–2497.
- (27) Minard-Basquin, C.; Chaix, C.; Pichot, C.; Mandrand, B. *Bioconjugate Chem.* **2000**, *11*, 795–804.
- (28) Beyer, D.; Bohanon, T. M.; Knoll, W.; Ringsdorf, H.; Elender, G.; Sackmann, E. *Langmuir* **1996**, *12*, 2514–2518.
- (29) Heba-Laref, F.; Mouzali, M.; Abadie, M. J. M. *J. Appl. Polym. Sci.* **1999**, *73*, 2089–2094.
- (30) Zhao, M.; Liu, Y.; Crooks, R. M.; Bergbreiter, D. E. *J. Am. Chem. Soc.* **1999**, *121*, 923–930.
- (31) Zhou, W.; Dong, J. H.; Qiu, K. Y.; Wei, Y. *J. Polym. Sci., Part A: Polym. Chem.* **1998**, *36*, 1607–1613.
- (32) Zhou, W.; Dong, J. H.; Qiu, K. Y.; Wei, Y. *J. Appl. Polym. Sci.* **1999**, *73*, 419–424.
- (33) Standard Specification for Skier Goggles and Faceshields: Annex A1. Test Method for Fogging Properties; F659-06; ASTM International: West Conshohocken, PA, 2004; p 145.
- (34) Chevallier, P.; Castonguay, M.; Turgeon, S.; Dubrulle, N.; Mantovani, D.; McBreen, P. H.; Wittmann, J. C.; Laroche, G. *J. Phys. Chem. B* **2001**, *105*, 12490–12497.
- (35) Horcas, I.; Fernández, R.; Gómez-Rodríguez, J. M.; Colchero, J. G.-H., J.; Baro, A. M. *Rev. Sci. Instrum.* **2007**, *78*, 013705.
- (36) Swanepoel, R. *J. Phys. E: Sci. Instrum.* **1983**, *16*, 1214–1222.
- (37) Vallières, K.; Chevallier, P.; Sarra-Bournet, C.; Turgeon, S.; Laroche, G. *Langmuir* **2007**, *23*, 9745–9751.
- (38) Gengenbach, T. R.; Griesser, H. J. *Surf. Interface Anal.* **1998**, *26*, 498–511.
- (39) Holvoet, S.; Chevallier, P.; Turgeon, S.; Mantovani, D. *Materials* **2010**, *3*, 1515–1532.
- (40) Freudenberg, U.; Zschoche, S.; Simon, F.; Janke, A.; Schmidt, K.; Behrens, S. H.; Auweter, H.; Werner, C. *Biomacromolecules* **2005**, *6*, 1628–1634.
- (41) Grombe, R.; Gouzy, M. F.; Freudenberg, U.; Pompe, T.; Zschoche, S.; Simon, F.; Eichhorn, K.-J.; Janke, A.; Voit, B.; Werner, C. *eXPRESS Polym. Lett.* **2009**, *3*, 733–742.
- (42) Pompe, T.; Zschoche, S.; Herold, N.; Salchert, K.; Gouzy, M. F.; Sperling, C.; Werner, C. *Biomacromolecules* **2003**, *4*, 1072–1079.
- (43) Tasso, M.; Cordeiro, A. L.; Salchert, K.; Werner, C. *Macromol. Biosci.* **2009**, *9*, 922–929.
- (44) Bratskaya, S. Y.; Simon, F.; Zschoche, S.; Synytska, A.; Marinin, D. V. *Polym. Sci., Ser. B* **2009**, *51*, 416–421.
- (45) Cristea, D.; Obreja, P.; Kusko, M.; Manea, E.; Rebigan, R. *Mater. Sci. Eng., C* **2006**, *26*, 1049–1055.
- (46) Pompe, T.; Renner, L.; Grimmer, M.; Herold, N.; Werner, C. *Macromol. Biosci.* **2005**, *5*, 890–895.
- (47) Briscoe, B. J.; Galvin, K. P. *Sol. Energy* **1991**, *46*, 191–197.
- (48) Pompe, T.; Kobe, F.; Salchert, K.; Jrgensen, B.; Oswald, J.; Werner, C. *J. Biomed. Mater. Res. A* **2003**, *67*, 647–657.
- (49) Grosu, G.; Andrzejewski, L.; Veilleux, G.; Ross, G. G. *J. Phys. D: Appl. Phys.* **2004**, *37*, 3350–3355.
- (50) Marmur, A. *Soft Matter* **2006**, *2*, 12–17.
- (51) Marmur, A. *Langmuir* **2003**, *19*, 8343–8348.